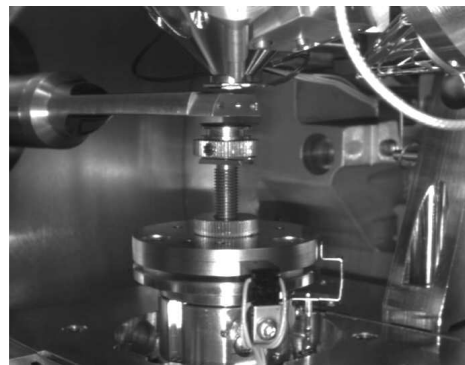
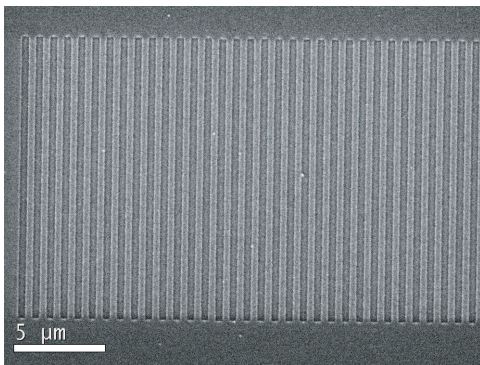


Cathodoluminescence Imaging Spectroscopy on Plasmonic Structures

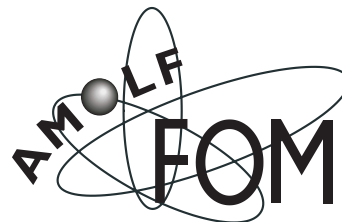
J.T. van Wijngaarden

Supervised by Prof. Dr. A Polman



Research project for the masters degree in
Experimental Physics at Utrecht University
August 2004 - August 2005

The Center for Nanophotonics
FOM-Institute AMOLF
Amsterdam



Abstract

Cathodoluminescence (CL) imaging spectroscopy is a powerful tool to investigate the optical properties of materials, with a resolution below the diffraction limit of light. In this thesis we report CL measurements on different classes of materials. CL measurements were done on rare earth doped materials that were in agreement with previous photoluminescence (PL) measurements on the same type of materials. In semiconductor materials, CL measurements could distinguish features of 100 nm, showing the high resolution of the system.

The focus of this thesis is on metal structures that were investigated with the CL system. Electrons can excite surface plasmons with a resolution much higher than can be achieved with optical excitation. In plain silver and gold films, surface plasmons can couple out by the roughness of the film, with a characteristic wavelength of the surface plasmon wavelength, radiative surface plasmons with a characteristic wavelength of the bulk plasmon wavelength are also observed. In gratings patterned in silver and gold, several peaks are observed that shift to the red for a larger grating period. We attribute these emission to localized surface plasmon modes in the grating ridges. Because of the high resolution of the CL system, we were able to measure propagation of surface plasmon near the surface plasmon resonance wavelength. For both silver and gold, the propagation length increased with wavelength a factor of 20 between the surface plasmon resonance and 200 nm higher. The data agreed with the calculations taking absorption in the film and roughness of the surface into account as loss mechanisms.

CL measurements on single gold nanoparticles showed dipole mode emission near the surface plasmon resonance for particles with diameter $d = 50\text{nm}$ and for a particle with $d = 110\text{nm}$ in addition to the dipole mode, higher order modes are observed, which is in agreement with previous results. Measurements on a cluster of particles showed slightly redshifted emission with respect to a single particle, which is attributed to longitudinal coupling of the plasmons in the particles.

Contents

1	Introduction	5
1.1	Electrons interacting with materials	5
1.2	Surface plasmons and electrons	6
1.3	This thesis	6
2	CL setup and characterization	9
2.1	Introduction	9
2.2	Setup	9
2.3	Results	11
2.3.1	Spectral information	11
2.3.2	CL imaging	14
3	CL on semiconductor materials	17
3.1	Introduction	17
3.2	Electrons interacting with semiconductors	17
3.3	Quantum confined semiconductors	18
3.4	Results	19
3.4.1	Quantum wells	19
3.4.2	Quantum dots	20
3.4.3	nanowires	21
4	Surface plasmons in metal films	23
4.1	Introduction	23
4.2	Fabrication and characterization	25
4.3	Localized surface plasmon modes	26
4.3.1	Radiation by surface roughness	26
4.3.2	Surface plasmon modes in gratings	28
4.4	Measuring the propagation of surface plasmons	30

5	Surface plasmons in metal nanoparticles	35
5.1	Introduction	35
5.2	Theory	36
5.3	CL spectroscopy on single particles	37
5.4	Coupling between metal nanoparticles	38

Chapter 1

Introduction

1.1 Electrons interacting with materials

Electrons can be used to characterize materials in many ways. Interactions of keV electrons with matter lead to different signals, for example secondary electrons, backscattered electrons, x-rays and photons in the ultraviolet, visible and infrared spectral range (see figure 1.1). This last process is called cathodoluminescence (CL) and can be defined as the emission of light as the result of electron (“cathode ray”) bombardment. [1] A very well known example of cathodoluminescence is the cathode ray tube, used in television screens, where luminescing phosphors are irradiated with an electron beam.

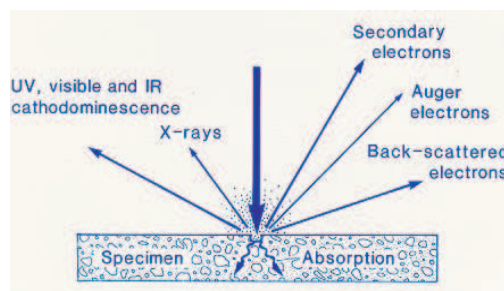


Figure 1.1: Schematic representation of different processes induced by keV electrons.

An advantage of CL compared to other forms of luminescence, like photoluminescence (PL) is the high spatial resolution that can be achieved. The typical diameter of an electron beam is in the order of nanometers and the interaction volume of such a beam is in the order of 100 nm, which is at least one order of magnitude smaller than the spot of a typical laser beam. By varying the beam energy one can also obtain depth resolved information, as the range

of the electrons is directly proportional to the beam energy.

CL has a wide variety of applications, in geology it is used for the investigation of rock compositions. In material science CL can be used to characterize the defects of the material [2] and the high resolution makes CL an ideal tool in nanosciences, to investigate the properties of for example nanowires [3].

1.2 Surface plasmons and electrons

When thin metal films are bombarded with high energy electrons, instead of cathodoluminescence a different effect occurs, which is the excitation of plasma oscillations, in the free electron gas in the metal. In the 1950's electron energy loss spectroscopy (EELS) measurements showed that fast electrons passing through metal foils did not experience random loss, which would be expected from scattering. Instead the loss spectra showed characteristic maxima, the so-called eigenlosses, which were attributed to the excitation of plasma oscillations, or plasmons. This effect was theoretically first described by Ritchie [4] in 1957, and he predicted the existence of surface plasmons, that have a lower characteristic energy than the bulk plasmons: $\omega_{sp} = \omega_p/\sqrt{2}$. Powell and Swan verified for an aluminium/air the existence of the surface plasmons with EELS [5]. Since then surface plasmons are studied both with electrons and optically, on both smooth and corrugated surfaces. Due to the prediction and experimental verification [6] of micrometer propagation, surface plasmons are now believed to have applications in optoelectronic devices. Therefore the field of plasmonics is now a rapid expanding field, in which the majority of research is done with optical instruments. However because plasmonic structures very often have subwavelength feature sizes, there still is a need for high resolution characterization. Present used scanning electron microscopes (SEMs), with beam diameters of several nanometers give the opportunity to excite surface plasmons at a well defined position with dimensions far below the diffraction limit of light, in combination with a cathodoluminescence setup to image the surface plasmons.

1.3 This thesis

This thesis can be divided in two parts. In the first part cathodoluminescence imaging spectroscopy will be introduced as a general technique, to investigate the optical properties of luminescing materials. The system is new in our laboratory and in chapter 2 will report on characterization of the CL system, that was performed during a demonstration in September 2004. The measure-

ments were done with rare earth doped materials, and a comparison between the CL measurements and earlier PL measurements could be made. Chapter 3 will present CL measurements on semiconductor materials that were done in collaboration with other research groups. It will also give a short introduction to the interaction of electrons with semiconductor materials.

The second part of this thesis will introduce cathodoluminescence as a technique to investigate plasmonic structures. Chapter 4 will report on surface plasmons in thin metal films. First a short introduction to surface plasmons in metal films will be given, then the properties of surface plasmons in planar films, with surface roughness and surface plasmons in gratings will be investigated. Finally the propagation of surface plasmons in metal films will be measured, for short wavelengths. This is difficult to do with optical methods, because propagation lengths are short and high resolution measurement techniques are required. CL imaging spectroscopy will be shown to be such a technique. In chapter 5 preliminary measurements on metal nanoparticles will be shown. These particles are interesting because the plasmon resonances can be confined to several nanometers in such particles. We will show that we are able to measure the properties of metal particles with a diameter below 50 nm.

Chapter 2

CL setup and characterization

2.1 Introduction

Buying a new type of equipment never happens before you know what actually the ability of the setup is. This chapter reports the characterization of the cathodoluminescence setup, that was done during a demonstration in September 2004. Measurements on different luminescing materials were performed, from which most properties were also known from photoluminescence spectroscopy. Therefore sometimes a comparison will be made between older PL results and the CL results from the demonstration measurements. First the CL setup itself will be discussed.

2.2 Setup

Figure 2.1 schematically shows the excitation and collection of light. A CL system is an extension to either a TEM or SEM. The results presented here are obtained in a Jeol 6300 SEM (Data presented in the other chapters is obtained in a FEI XL 30 SEM). An aluminium parabolic mirror is placed between the sample stage and the pole pieces. Through a hole in the mirror, the sample is irradiated with electrons and the luminescence is collected. For the most efficient collection, the sample must be in the focal point of the mirror, which is 1 mm below the mirror itself. Because of the parabolic shape, the mirror reflects the light as a parallel beam into a waveguide. The detection of the light by the MonoCL3 system can occur in two modes. In the panchromatic mode all the emitted light is collected by the detector, while in the monochromatic mode the light is led through a monochromator, which allows one to take a spectrum, or make an image at one particular wavelength. Two mirrors are used for switching between these modes. The monochromator is a Czerny Turner type

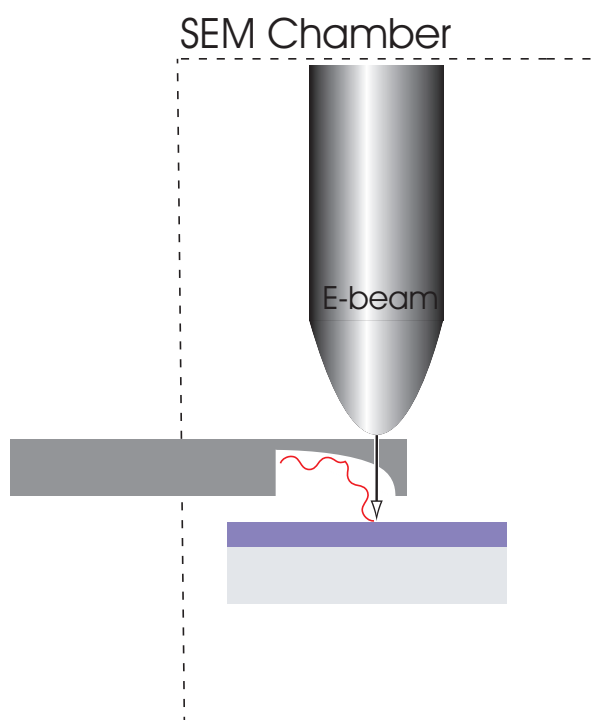


Figure 2.1: Schematic representation of the detection of light with the parabolic mirror from the CL system. The waveguide attached to the mirror guides the light either to the spectrometer or directly to the detector.

and contains two gratings, one blazed at 500 nm with 1200 lines/mm and one blazed at 1600 nm with 600 lines/mm (See for specifications table 2.1) .

The system is configured with two detectors, which together with the grating response cover a wavelength range of 300 – 1800 nm. A peltier cooled high sensitivity photo multiplier tube (HSPMT) has a response between 160 – 930 nm. The germanium infrared detector is cooled with liquid nitrogen and has a response from 800 – 1800 nm. Together with the blazed gratings, this gives a typical response for the system that is shown in figure 2.2.

In the near future, the system will be extended with a CCD array detector, that allows one to collect spectra in a fraction of the time used now. Furthermore a polarization filter will be inserted just after the waveguide and a filter housing will be placed just before the detectors. This enables one to select a certain spectral band, without using the monochromator.

Monochromator type	Czerny Turner
Focal length	300 mm
Dispersion	$1.8 \times 1800/\text{ruling density (nm/mm)}$
Grating size	$69 \times 69 \text{ mm}^2$
Entrance, exit slits	0 – 10 mm
Min. step size	Grating dependent, 0.1 nm for high resolution

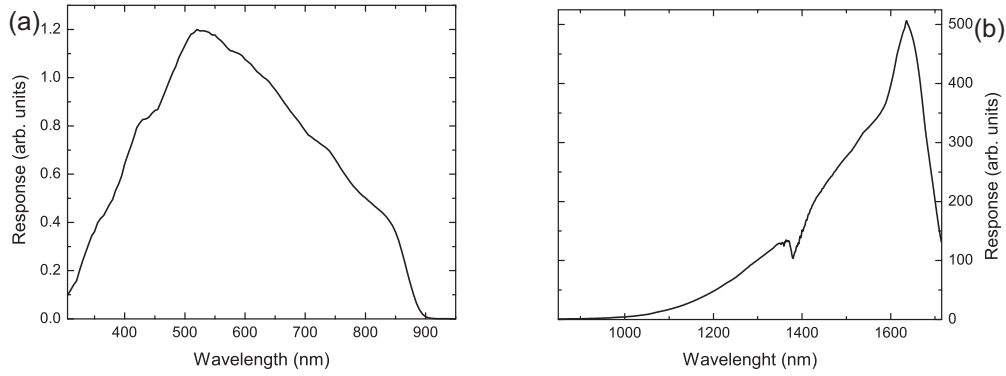
Table 2.1: Monochromator specifications

Figure 2.2: System response of the HSPMT with the 500 nm blazed grating (a) and the germanium detector with the 1600 nm blazed grating (b). (a) is smoothed using adjacent averaging.

2.3 Results

The presented results will give an idea of the possibilities and different techniques of the CL system. During the demonstration, samples with already known optical properties were investigated, and sometimes a comparison between CL and PL can be made. The spectra presented in this chapter are not corrected for the system responses, shown in figure 2.2.

2.3.1 Spectral information

Figure 2.3 (a) shows the CL spectra of silica colloids, a thin silica film, and a thin silicon rich oxide (SiO_x , $x < 2$) film, all doped with erbium (black line, grey line divided by 5 and light grey line respectively). All spectra peak near $1.53 \mu\text{m}$, the characteristic ${}^4\text{I}_{13/2} \rightarrow {}^4\text{I}_{15/2}$ transition of Er^{3+} . Absolute intensities cannot be compared due to different beam currents (which are unknown). As comparison figure 2.3 (b) shows a PL spectrum of the erbium doped silica colloids, excited with a 488 nm laser. The PL spectrum also peaks at $1.53 \mu\text{m}$, but it clearly has a higher spectral resolution.

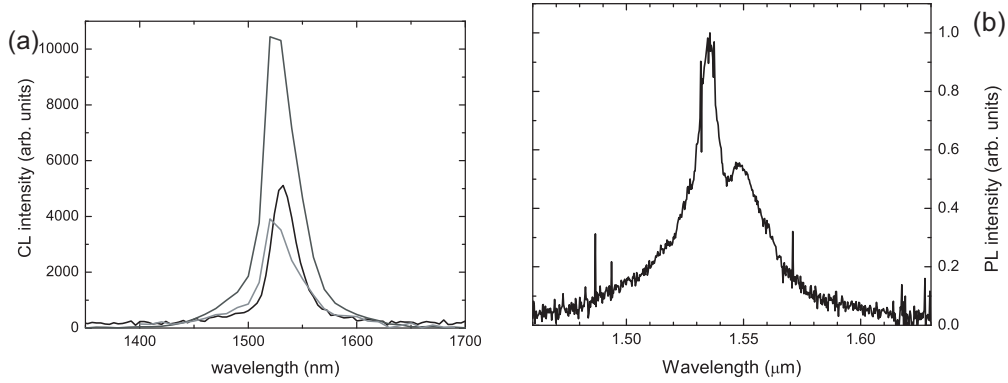


Figure 2.3: (a) CL spectra of uniform erbium doped silica colloids (black line), silica film (grey line, divided by 5) and a silicon rich oxide film (light grey line). (b) Normalized PL spectrum from uniform erbium doped silica colloids, taken from [7].

Figure 2.4(a) shows a CL spectrum of an Er-Si-O complex, made as described in ref. [8], in both visible and infrared spectral range. The inset shows a panchromatic CL image of the structure. This sample also shows characteristic Er^{3+} luminescence at $1.53 \mu\text{m}$, and in addition luminescence peaks at 980, 660 and 540, 460, 410 and 380 nm are observed. The maxima correspond to the $^4\text{I}_{13/2}$, $^4\text{I}_{11/2}$, $^4\text{F}_{9/2}$, $^4\text{S}_{3/2}$, $^4\text{F}_{5/2}$, $^2\text{H}_{9/2}$, and the $^4\text{G}_{11/2}$ transitions respectively (see fig. 2.4 (b)). These transitions were not observed in the colloids, silica thin films and silicon rich oxide thin films doped with erbium (data not shown). The difference is attributed to the differences in phonon energy of the host material. If an energy gap between an excited state and a lower state is smaller than typically six times the phonon energy of the host material, the transition occurs non-radiatively; the typical phonon energy in SiO_2 is higher than in the Er-Si-O complex.

Terbium is a rare earth ion which emits light in the visible region. Figure 2.7 shows the spectrum of silica colloids doped with terbium, measured with CL (a) and PL (b), excited with a 488 nm laser. The peaks at 488 nm and higher wavelengths correspond to transitions between the $^5\text{D}_4$ level, and different lower states. All peaks are due to characteristic transitions in Tb^{3+} (with exception of an unidentified peak at 570 nm in the PL spectrum). Peaks with a wavelength of 488 nm and lower are only observed in the CL spectrum, as PL was excited at 488 nm.

Silicon nanocrystals a broad PL peak between 700 – 900 nm. An often used fabrication process, is to implant a silica substrate with silicon and to anneal the sample, to form the nanocrystals. CL measurements were done on two samples doped with nanocrystals, a thin silica film, and a silica ring resonator.

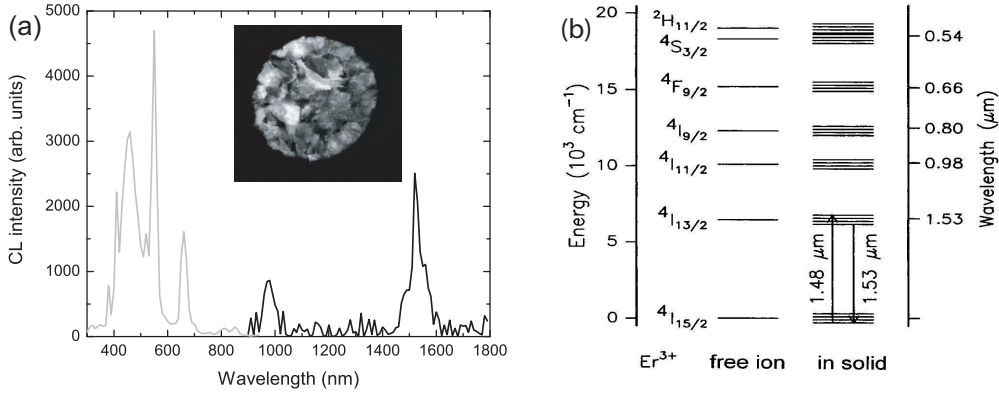


Figure 2.4: (a) Joined spectra from HSPMT and Ge detector, of an Er-Si-O complex (shown at the inset). The different peaks correspond to the energy levels from the diagram of (b) (taken from [9].)

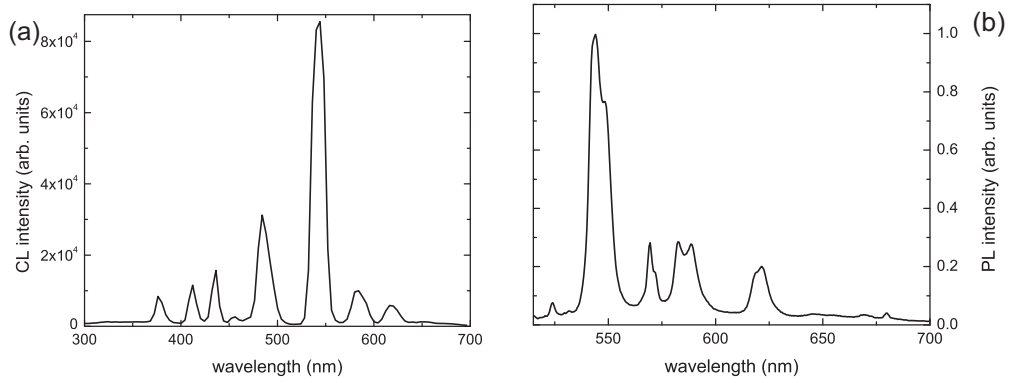


Figure 2.5: Spectra of $\text{SiO}_2 : \text{Tb}$ colloids, obtained with CL (a) and PL (b), excited at 488 nm. ((b) taken from [7])

Figure 2.6 shows for both samples a maximum at $\lambda = 460$ nm, which is not the expected nanocrystal luminescence wavelength. This broad emission may be caused by irradiation related defects, created during the silicon implantation.

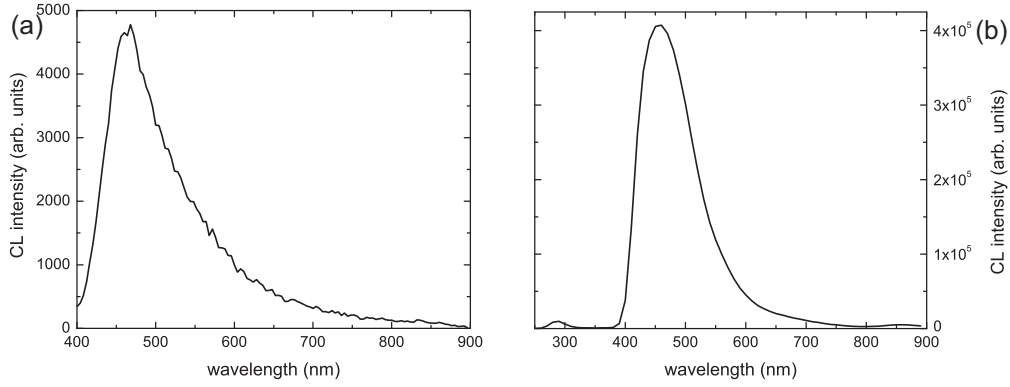


Figure 2.6: Spectra of silica thin film a) and silica ring resonator b) doped with silicon nano crystals.

2.3.2 CL imaging

As stated before, the CL system has two collection modes, monochromatic and panchromatic mode. For information on luminescence at one particular wavelength the monochromatic mode can be used. A disadvantage is that the intensity decreases dramatically and the widest possible band to look at is 27 nm in the visible regime and 54 nm in the infrared regime. In future a different possibility will be to insert a filter in the light path in panchromatic mode. In this way it will be possible to select a wider spectral band, or block a certain regime, for example to get rid of the defect related luminescence.

Figure 2.7 shows both panchromatic (a) and monochromatic (b) images of terbium doped colloids. The intensity difference can be seen very clearly. From the monochromatic image it also seems that most luminescence comes from the outer part of the colloids, which would mean that the largest amount of terbium is concentrated in the outer shell of the colloids. Both images contain a step as if the beam suddenly shifted to a different area. A possible explanation is drift in the sample due to external vibrations, or charging of the silica colloids which causes the beam to drift away. This last effect can be reduced with a faster scanning time.

Figure 2.8(a) shows the panchromatic image of erbium doped silica colloids. The light in this image is emitted at $1.54\mu\text{m}$ (see corresponding spectrum in fig. 2.3(a)). Due to the long lifetime of erbium (about 10 ms), the colloids have a luminescing tail in this image. This image is collected with a pixel time

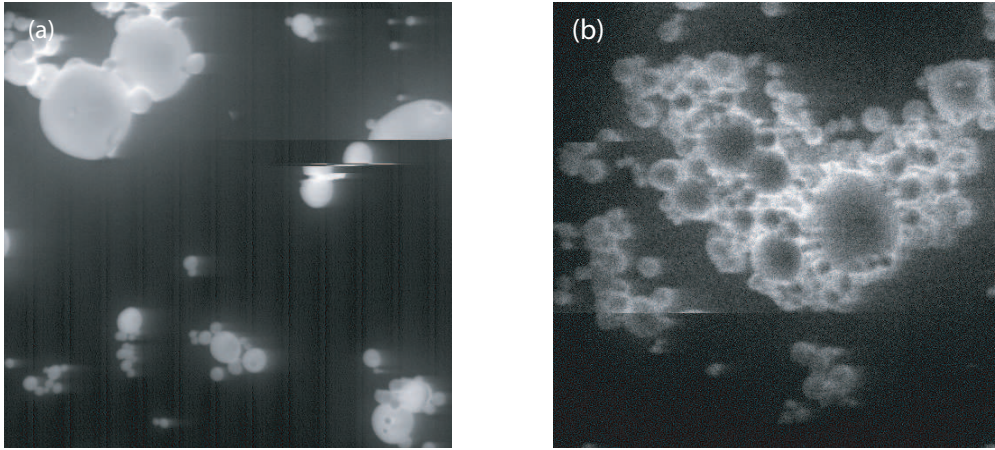


Figure 2.7: Images of silica colloids doped with terbium, diameter of the colloids is in the order of μm . (a) All light from the sample is collected (panchromatic mode). (b) Luminescence at $544 \pm 4 \text{ nm}$ (monochromatic mode). The sudden steps in the images can be explained by drift of the beam or the sample.

of 1 ms/pixel, thus the erbium is still luminescing while the beam has moved away. The system addresses the light to a spot next the colloid, resulting in the light tails. By increasing the time per pixel this effect is reduced, but on the other hand, it can be used to calculate the lifetime of erbium. It is very easy to convert this image in an intensity spectrum per pixel, along a line, or several lines averaged (the red rectangle in fig 2.8(a)). Using the pixel dwell time of 1 ms/pixel a decay trace is constructed (fig. 2.8(b)). An exponential fit to this data gives the $1/e$ decay time $\tau = 14.34 \pm 0.49 \text{ ms}$, which is close to the typical value of 13.5 ms in erbium doped silica colloids [7].

Charging of the sample limits the imaging possibilities. A good example of charging can be seen in figure 2.9, where waveguides in $\text{Al}_2\text{O}_3 : \text{Er}$ are shown. This material is a very good insulator and it is almost impossible to collect an image of this sample. Decreasing the beam current or the beam energy will reduce the charging, but this will also lower the intensity of the light.

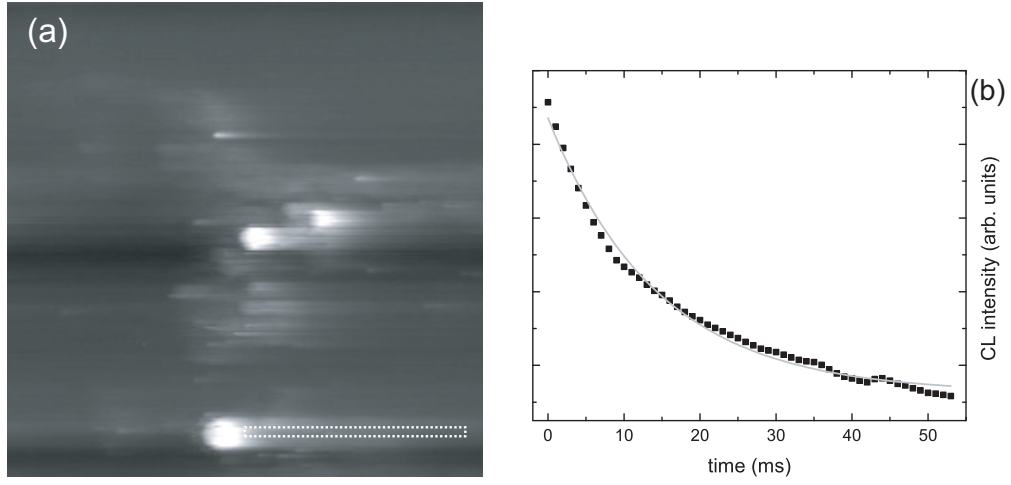


Figure 2.8: (a) Panchromatic image of erbium doped silica colloids, collected with the Ge-detector. The tails in the image are caused by the long lifetime of erbium in combination with the high sensitivity of the detector. This image can be used to calculate the lifetime of erbium. (b) Erbium decay trace obtained from the image and exponential fit on the data. The calculated lifetime of erbium is: $\tau = 14.34 \pm 0.49\text{ms}$.



Figure 2.9: Panchromatic image of the waveguides in $\text{Al}_2\text{O}_3:\text{Er}$, with clearly visible charging effects.

Chapter 3

CL on semiconductor materials

3.1 Introduction

Cathodoluminescence imaging and spectroscopy is used in a wide range of research, from geology to nano technology. It is beyond the scope of this thesis to cover the applications of CL in these fields of research. However before focussing on the use of CL in surface plasmon research an overview of measurements performed on semiconductor materials will be presented in this chapter. Also the theoretical background of interaction of electrons with semiconductor will be discussed.

3.2 Electrons interacting with semiconductors

The advantage of Cathodoluminescence over other luminescence techniques is the high spatial resolution of CL. In semiconductors this is determined by the interaction or generation volume of the incident electrons, which is the volume in which the incident electrons undergo a series of elastic and inelastic scattering events. The events result in electron-hole pair generation, x-rays and cathodoluminescence. The depth to which these events happen is described by the electron range, which is in its most general form derived by Kanaya and Okayama [10]:

$$R_e(\mu m) = \left(0.0276 A / \rho Z^{0.889}\right) E_b^{1.67}, \quad (3.1)$$

with E_b the electron energy in keV, A the atomic weight in g/mol, ρ the material density in g/cm³ and Z the atomic number. For 5 keV electrons in silicon this gives an electron range of 0.47 μm . Figure 3.1 shows simulations on the electron generation volume in silicon and gallium nitride for 5 keV electrons.

The contours indicate the fraction of incident beam energy left at that position. Note that the scale is different; the maximum width of the generation volume in silicon is 400 nm, while in gallium nitride it is 150 nm. Because the $A/Z^{0.889}$ roughly remains constant for different materials, the difference in generation volume is mainly caused by the density differences between Si ($\rho = 2.33 \text{ g/cm}^3$) and GaN ($\rho = 6.10 \text{ g/cm}^3$).

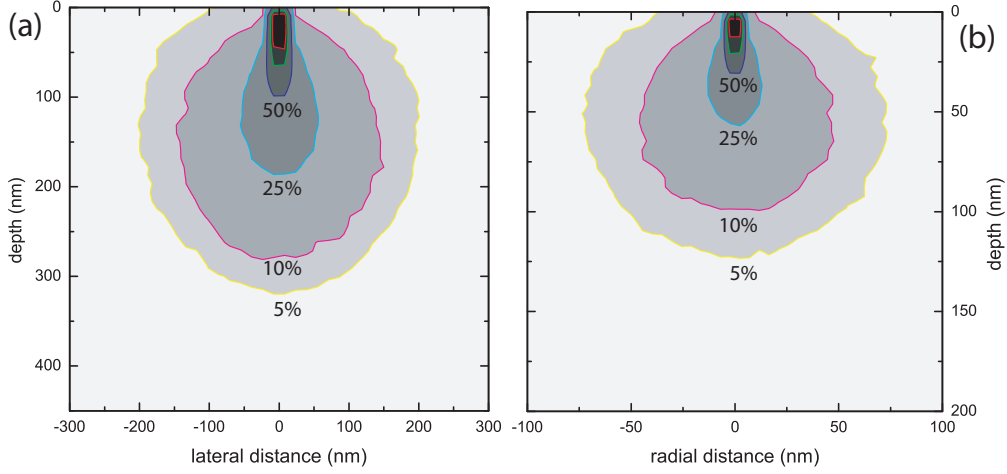


Figure 3.1: Electron energy distribution for 5 keV electrons in (a) silicon and (b) gallium nitride. ((a) and (b) not on the same scale)

The generation of electron-hole pairs by electrons is different than that by photons. While a photon generates only one electron hole pair, an electron can generate up to thousands of electron-hole pairs in a generation volume. The creation of a single electron hole pair, by electrons requires an energy of approximately three times the band gap, independently of the incident electron energy [11, 12]. The local generation rate of electron-hole pairs is given by [13]

$$G = \frac{E_b I_b Q (1 - \gamma)}{e E_g}, \quad (3.2)$$

where I_b is the beam current, e is the electronic charge, γ is the backscatter coefficient, E_g is the band gap energy and Q is the quantum efficiency for electron-hole pair generation.

3.3 Quantum confined semiconductors

If a semiconductor has in at least one direction dimensions in the order of a few nanometer, different behavior will be seen compared to bulk semiconductors, because quantum mechanical effects come to play a role. This is why one also speaks of quantum confined semiconductors. Quantization of energy levels

occurs, which can be understood from solving the Schrodinger equation for a particle in an infinite square well. In contrast to a bulk semiconductor where there is a continuum of possible energies, in a confined semiconductor, the energy levels are separated, given by:

$$E_n = \frac{n^2 \pi^2 \hbar^2}{2ma^2}, \quad (3.3)$$

with m the mass of the particle and a the width of the well, or in our case the size of our semiconductor. If the semiconductor becomes larger, the separation between the energy levels will be smaller, and in the limit of bulk materials there is again a continuum in energies. Another consequence of the small size of the semiconductor is the shift in bandgap energy. A bound electron-hole pair, or exciton, can be viewed as an electron orbiting a hole at a certain distance, which is in analogy to the hydrogen atom, the Bohr radius of the exciton. If the size of the semiconductor approaches the Bohr radius of the exciton, the electron-hole pair is spatially confined, and the exciton energy increases.

Quantum wells, nanowires and quantum dots are quantum confined semiconductors in one, two and three dimensions. To study these materials on the nanometer scale, CL is a very practical tool, as will be illustrated in the next section.

3.4 Results

3.4.1 Quantum wells

In quantum wells, charge carriers are trapped in a thin planar region in the semiconductor. Often several quantum well layers are used, separated by a larger bandgap material. Quantum wells are used in for example diode lasers. The structure shown in figure 3.2 consists of five double layers of 5 nm In-GaN/10 nm GaN. These are embedded in a 200 nm GaN:Si layer at the surface and two 1 μ m GaN layers under the structure. The emission wavelength of the quantum well structure is 477 nm, and the two GaN layers emit at 360 nm. A panchromatic image of the cross section is shown, indicating the scan path of the linescans with the line. Linescans are collected at the emission wavelength of GaN at 360 nm, and at 477 nm, the emission wavelength of the quantum well. Clear variations in intensity are observed for the GaN CL. The intensity dip in the 360 nm intensity profile may be caused by defects due to the breaking of the sample, or surface defects that are created during the growth of the different layers. The CL from the quantum wells is clearly visible near the surface .

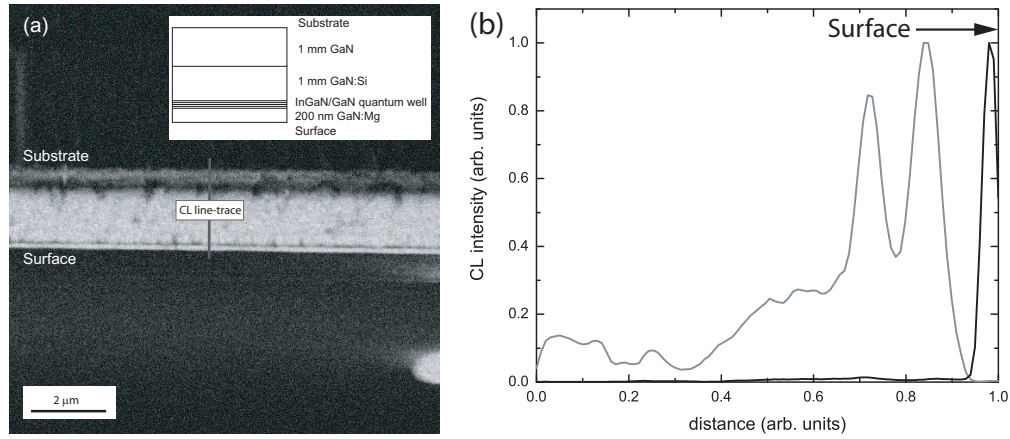


Figure 3.2: (a) Panchromatic CL image of the layered structure, beam energy 5 keV, beam current ... pA, inset shows schematic representation. (b) Intensity profiles from linescan in (a), collected at 360 nm (grey line) and 477 nm (black line).

3.4.2 Quantum dots

Because the tunability of the emission wavelength, quantum dots are frequently used as light emitters or fluorescent labels. A thick layer of CdSe quantum dots was spin coated on either an ITO coated silica glass sample or an Ag coated silicon wafer. Figure 3.3 (a) shows the spectra of quantum dots on the silver layer, for electron beam energies of 5 (grey line) and 30 keV (black and light grey lines). For the 30 keV electrons a spectrum with a large and a small scan area are collected. The larger intensity for the large scan area indicates that the quantum dots are efficiently excited, and thus the larger the scan area, the larger the luminescence intensity. The peak intensity for 5 keV electrons is higher than for 30 keV electrons scanning a small area. This is because most part of the generation volume for 30 keV electrons is below the layer with quantum dots, which is about 1 μm thick. As a consequence of the electron irradiation, the luminescence intensity decreases. Figure 3.3 (b) shows three spectra obtained at the same position on the sample. Each spectrum took 100 seconds, and the dose was 1.5 nA/cm². These measurements were done on a different sample than those shown in figure 3.3 (a). The broad emission peak can be due to the poly dispersity of the quantum dots. It can be either charging or damage to the quantum dots that cause the intensity decrease.

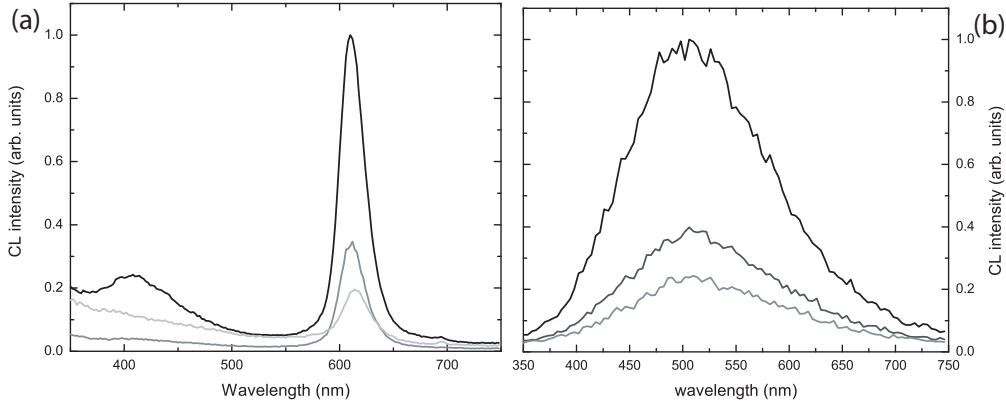


Figure 3.3: (a) Luminescence spectra from CdSe quantum dots emitting at 610 nm. Used electron beam energies: 30 keV large scan area (black line), 30 keV small scan area (light grey line) and 5 keV (grey line). (b) CL intensity from CdSe quantum dots, measured several times on the same position, show intensity decrease due to electron beam irradiation.

3.4.3 nanowires

Figure 3.4 shows results from CL measurements on ZnO nanowires, with diameters in the order of a hundred nanometers. Hence quantum effects do not play a role anymore, but still larger wires can play an important role in for example the design of miniature lasers. In (a) the spectra are shown from the nanowires on silica (grey line) and on gold (black line). The spectrum from the nanowires on gold show that two luminescence peaks are observed, uv emission at 380 nm and defect related emission from the nanowire centered around 500 nm. For the nanowires on silica, defect luminescence from the substrate (the peaks at 450 and 650 nm) dominates. In (b) a CL line trace on a single nanowire shows submicrometer intensity variations along the wire.

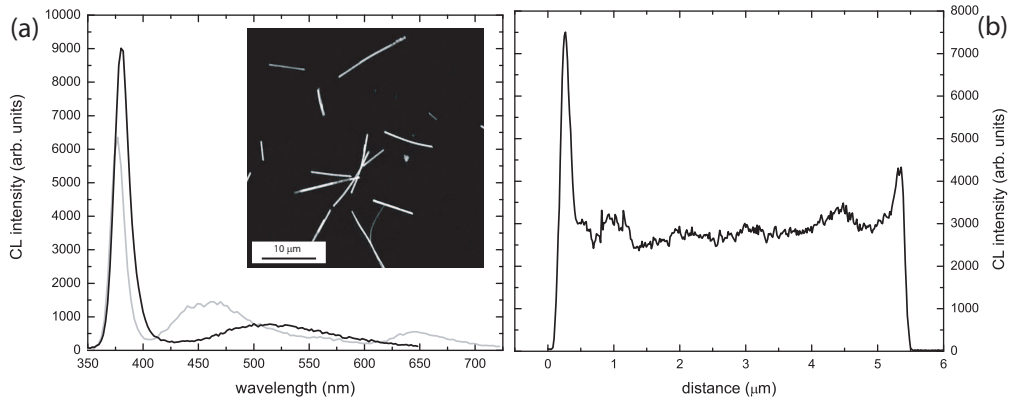


Figure 3.4: (a) Spectra from a single nanowire on silica (grey line) and gold (black line), and panchromatic image of nanowires on silica (inset). The broad luminescence peak at 500 nm is defect related luminescence from the nanowire, while the peaks at 450 and 650 nm are defect luminescence from the silica substrate. (b) CL line trace along a single nanowire at 380 nm. Submicrometer variations in intensity can be measured this way.

Chapter 4

Surface plasmons in metal films

4.1 Introduction

A surface plasmon is a bound electromagnetic wave at a metal dielectric interface, due to coherent electron oscillations in the metal which decays exponentially perpendicular from the surface. The electric field of the surface plasmon is described by

$$E(x, z, t) \sim E_0 \exp[i(k_x x - k_z |z| - \omega t)], \quad (4.1)$$

with k_z imaginary to have the exponential decay of the electric field, perpendicular to the surface. Solving Maxwell's equations with the proper boundary conditions, and assuming a complex dielectric function in the metal $\varepsilon_m = \varepsilon'_m + i\varepsilon''_m$, gives the dispersion relation for $k_x = k'_x + ik''_x$ [14]

$$k'_{sp} = \frac{\omega}{c} \sqrt{\frac{\varepsilon_d \varepsilon'_m}{\varepsilon_d + \varepsilon'_m}}, \quad (4.2)$$

$$k''_{sp} = \frac{\omega}{c} \left(\frac{\varepsilon_d \varepsilon'_m}{\varepsilon_d + \varepsilon'_m} \right)^{3/2} \frac{\varepsilon''_m}{2(\varepsilon'_m)^2}. \quad (4.3)$$

For real k'_{sp} one needs $\varepsilon'_m < 0$ and $|\varepsilon_m| > \varepsilon_d$; k''_{sp} determines the internal absorption of the metal film, and thus gives an maximum propagation of the surface plasmon. k'_{sp} is plotted in figure 4.1 for a silver-air interface, using measured values of the dielectric constant in the metal ε_m , together with the light line, $\omega = ck_x$. Figure 4.1 shows that for small k_x , the dispersion of surface plasmons approaches the light line. At values near the surface plasmon resonance ω_{sp} , surface plasmons have a significantly larger k_x than photons have, in other words, the wavelength of surface plasmons is shorter than the wavelength of photons of the same energy. It is this feature that makes surface plasmons attractive in the field of nanophotonics, because it helps one to

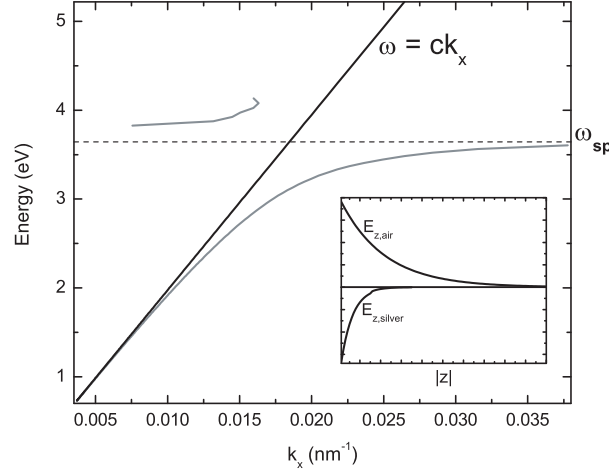


Figure 4.1: Dispersion relation of a surface plasmon at a silver air interface (grey line), plotted with the light line (black line). Inset: The electric field perpendicular to the silver air interface.

shrink the photon to dimensions smaller than its own wavelength, which may lead to the miniaturization of photonic circuits. Because of the smaller wavelength, or larger momentum than their photonic counterpart ($k_{sp} > k_{light}$), surface plasmons are non-radiative. For coupling to the far field one needs for example a grating to correct for the momentum mismatch, according to

$$k_x = \frac{\omega}{c} \sin \theta \pm nG, \quad (4.4)$$

with θ the angle at which the light couples out and G the grating vector $2\pi/a$, with a the grating period.

Left of the light line, for $E > \hbar\omega_p$ the dispersion curve for the radiative surface plasmons is shown. Contrary to non-radiative surface plasmons, these plasmon modes can couple to radiation, because their momentum is smaller than that of light [15]. The inset shows the perpendicular component of the electric field of the surface plasmon. This clearly shows that the field is exponentially decaying, and also that the field extends much more into the dielectric medium, than into the metal.

In this chapter CL measurements of surface plasmons in thin films will be presented. First surface plasmons in plain thin films with surface roughness and surface plasmon modes in gratings are investigated. We will also present CL as a tool to measure the propagation of surface plasmons near ω_{sp} , where propagation lengths are short.

4.2 Fabrication and characterization

The measurements described in this chapter are performed on silver and gold films, patterned with gratings ranging from 250 nm to 2 μm . The structures are written with e-beam lithography in a PMMA layer on a silicon wafer. Developing the exposed PMMA and etching with a SF_6 plasma for 50 seconds, the structure is written in the silicon. Due to the instability of the plasma, it is difficult to control the etching process. Therefore the depth of the gratings varies on different samples between 60 and 85 nm. By thermal evaporation, a metal layer is deposited on the silicon substrate. Figures 4.2 schematically shows the fabrication process and a SEM imaged grating in silver.

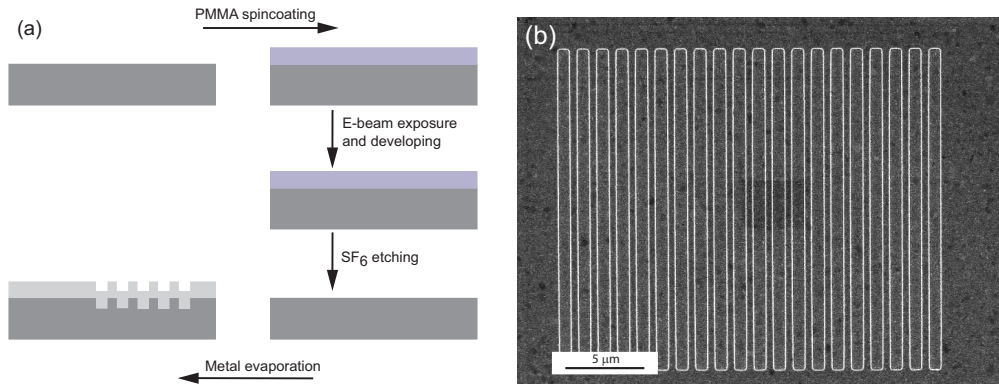


Figure 4.2: (a) Schematic fabrication process of a grating patterned metal film. (b) SEM imaged grating in silver.

Figure 4.3 (a) and (b) show the roughness of the film, measured with atomic force microscopy (AFM) and a cross section of the AFM image respectively. The roughness can be characterized with two parameters. The root mean square height δ which is given by

$$\delta = \sqrt{\frac{1}{A} \int_A z^2(x, y) dx dy}, \quad (4.5)$$

characterizes the roughness. From the AFM image we obtained $\delta = 3.7\text{nm}$. The correlation length σ is a measure how the roughness at one point is correlated to the roughness at another point. When $\sigma \rightarrow 0$ the roughness is completely random distributed. From the auto correlation function we estimated the correlation length to be $\sigma = 300\text{ nm}$. With ellipsometry the optical constants of the silver and the gold are obtained. Figure 4.3 (c) shows for both a silver and a gold film the results, which are in close agreement with tabulated data [16, 17]. From the optical constants the surface plasmon resonance wavelength at the metal-air interface, λ_{sp} can be obtained, from $\varepsilon'_{metal}(\lambda_{sp}) = -1$.

For silver this gives $\lambda_{sp} = 340\text{nm}$, and for gold $\lambda_{sp} = 361\text{nm}$. Both optical constants and surface roughness parameters are important in calculating the propagation length, as will be shown in section 4.4.

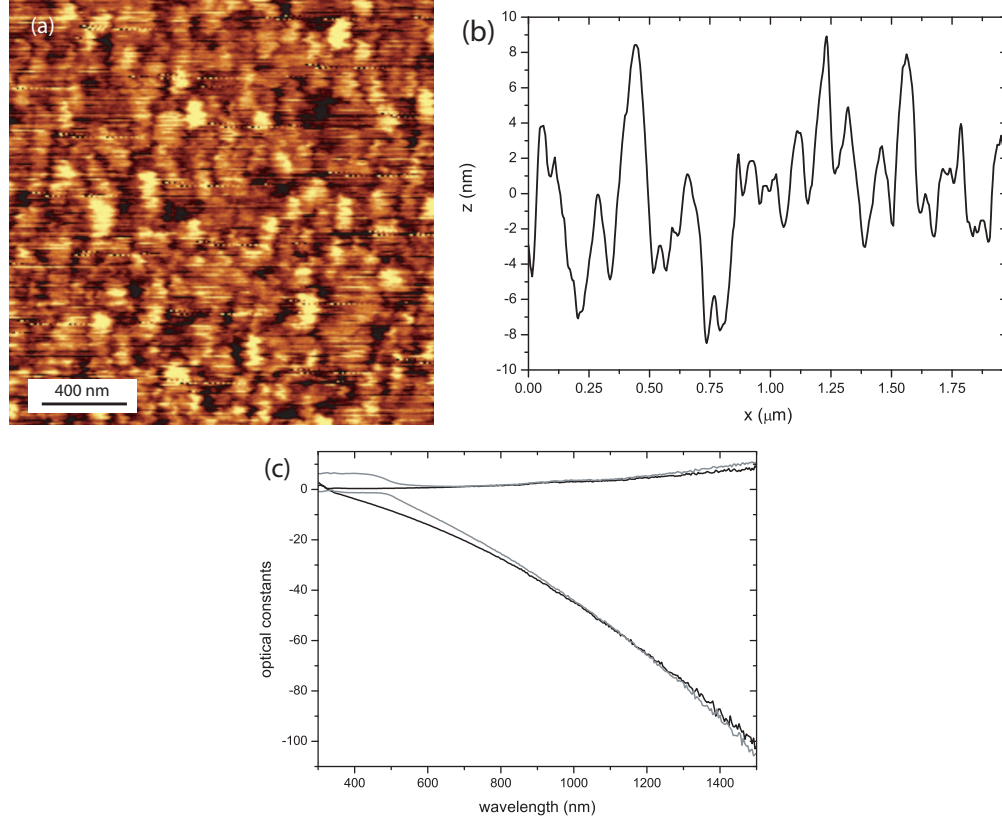


Figure 4.3: (a) AFM measurement on a silver film (b) Cross section of (a). (c) Optical constants measured using ellipsometry for a silver film (black line) and a gold film (grey line).

4.3 Localized surface plasmon modes

4.3.1 Radiation by surface roughness

At the surface plasmon resonance frequency ω_{sp} , surface plasmons do not propagate and one speaks of localized surface plasmon modes. Because these plasmons are not propagating, it is not possible to use a grating to couple them out. However surface plasmons can also couple to radiation by surface roughness. This mechanism which is a limiting factor in the propagation of surface plasmons can now be used to measure non propagating surface plasmon modes. When the localized plasmon is excited in the film, it directly radiates

back, due to the roughness of the film.

To study the effect of roughness on plasmon radiation in detail, CL measure-

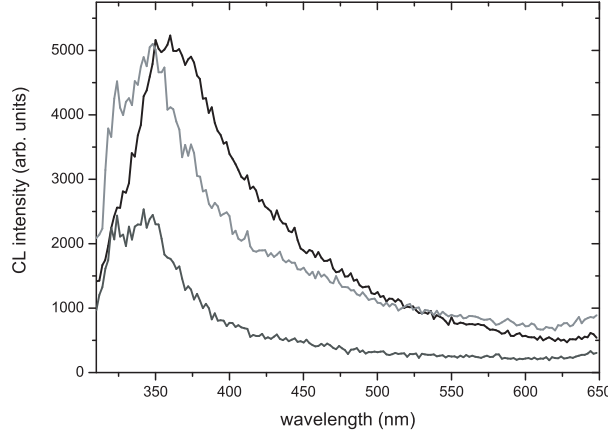


Figure 4.4: CL intensity on a random grating structure (black line), a scratch in the film (grey line) and on the plain silver film (dark gray line).

ments were performed on a plain silver film, a scratch in the film and a random patterned structure in the film. Figure 4.4 shows these CL spectra (dark grey, grey and black line respectively). The spectra peak close to the plasmon resonance wavelength of silver ($\lambda_{sp} = 340\text{nm}$), although the spectrum from the random structure is slightly redshifted. In addition a long tail is observed at all spectra, which may be related to surface plasmons at wavelengths larger than the surface plasmon resonance wavelength. The spectra from the plain films also have a small peak at 325 nm, which is the bulk plasmon wavelength ω_p , this emission comes from radiative plasmon modes. The intensity differences between the plain film and the scratch and random structure are caused by the increased roughness at the scratch and the edge of the random structure.

Figure 4.5 (a) shows a panchromatic CL image of the random structure in silver. The highest intensity comes from the edges in the structure, where the roughness is high. A monochromatic image of a silver film with a scratch, collected at $\lambda = 350\text{ nm}$, is shown in figure 4.5 (b). The highest intensity is again found at the edge of the scratch. Both effects in (a) and (b) are due to surface plasmons directly radiated to light. Bright spots also appear on the silver film, indicating the roughness by which the surface plasmon is radiated to light, but with significant lower intensity, as is also shown in figure 4.4.

Figure 4.6 shows CL spectra from a gold film, also taken at a random grating, a scratch and the plain film (black, dark grey and light grey line respectively). The spectra have a maximum at $\lambda \approx 550\text{ nm}$, which is slightly above the calcu-

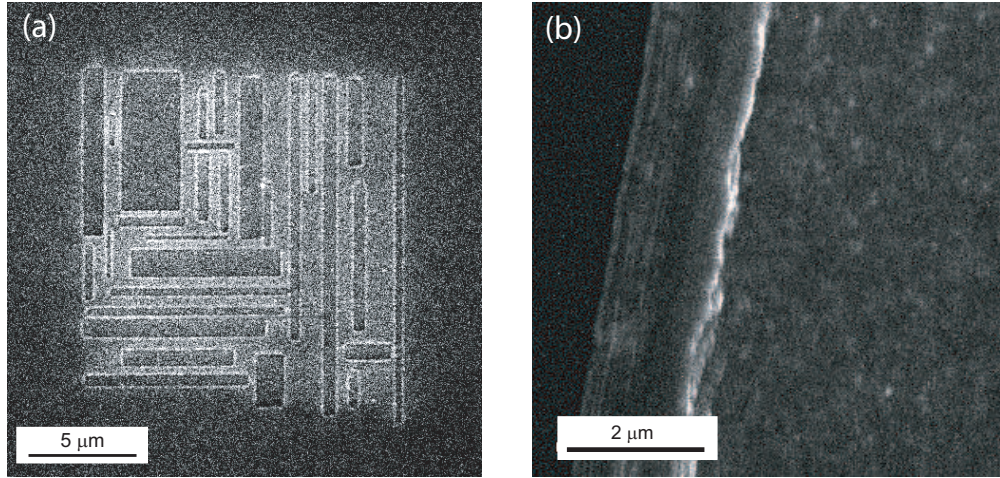


Figure 4.5: (a) Panchromatic CL image of the random patterned structure in the silver film. (b) Monochromatic CL image of the scratch in the silver film, collected at $\lambda = 350$ nm. At the sharp edges of the film, many light is coupled out. The lighter spots at the right of the scratch are due to surface roughness in the silver film.

lated surface plasmon wavelength for gold. A similar effect is thus found for silver and gold, but the intensity for the data from gold is smaller which may be caused by a smaller roughness of the gold film.

4.3.2 Surface plasmon modes in gratings

Gratings in thin metal films are used to couple surface plasmons to light, at a characteristic angle θ , according to:

$$k_x = \frac{\omega}{c} \sin \theta \pm nG. \quad (4.6)$$

Figure 5.5 shows for two grating periods (400 nm, grey line and 800 nm, black line) the angle at which the surface plasmon is coupled out in the first order ($n=1$) to the far field for a given wavelength. Since the collection mirror in the CL system collects all the light in a range of approximately $|\theta| < 10^\circ$, surface plasmon radiation over a large spectral area is collected. This range extends more to the red for a larger grating period.

To image surface plasmon radiation from gratings, a 30 keV electron beam is scanned over a part of the grating area. In a different setting the electron beam was defocused, to increase the spot size of the beam, with the spot positioned in the center of the grating. Both methods of excitation give the same qualitative result, with the highest intensity observed in the scanning mode. Samples with different grating periods were made and CL was collected from

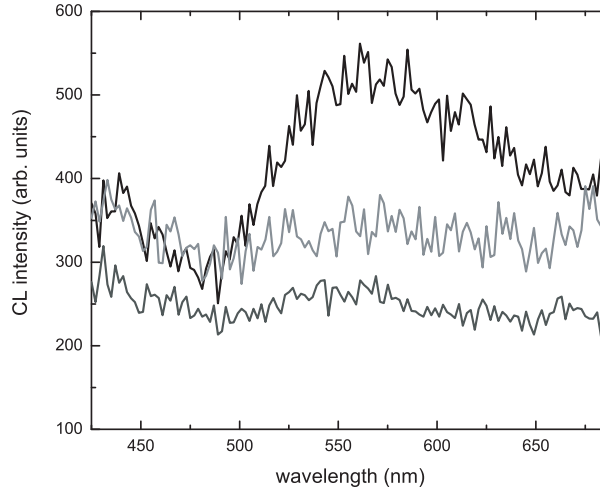


Figure 4.6: CL spectra measured on a gold film, with a random grating (black), scratch (dark grey) and the plain gold (light grey).

each of them. Figure 4.8 shows the spectra measured on silver and gold films grating pitches varying between 300 and 1000 nm. In both silver and gold, the emission spectra varies with the grating pitch, though in gold this effect is less pronounced. For silver in each spectrum a peak at $\lambda = 360$ nm is present, which is also observed in the spectrum of the random structure (see fig. 4.4). This emission is identified as surface plasmons coupled out by roughness. Besides this maximum other maxima appear, that shifts to higher wavelengths as the grating period increases. The four different peaks are marked, and figure 4.9 (a) shows how the energy of the emitted light at the peaks changes with grating period. These results shows similarities with CL measurements done by ref. [18] on silver nanoparticles. In this research, the different maxima are identified as localized multipole modes in the particles, that also shift to higher wavelengths as the diameter of the particle increases. Therefore we attribute our results to localized modes in the grating ridge, that change as either the distance between the ridges or the width of the ridge itself changes.

The results from the gold film show a similar effect. As in figure 4.6 each spectrum contains a maximum at $\lambda = 530$ nm, close to the surface plasmon resonance wavelength, and three other maxima can be identified as is shown in figure 4.9 (b). Due to the rapid decreasing detector efficiency above 700 nm, it is difficult to investigate if maxima at higher wavelengths occur. The peak at 694 nm, which is observed in each spectrum is due to Cr^{3+} pollution in the system.

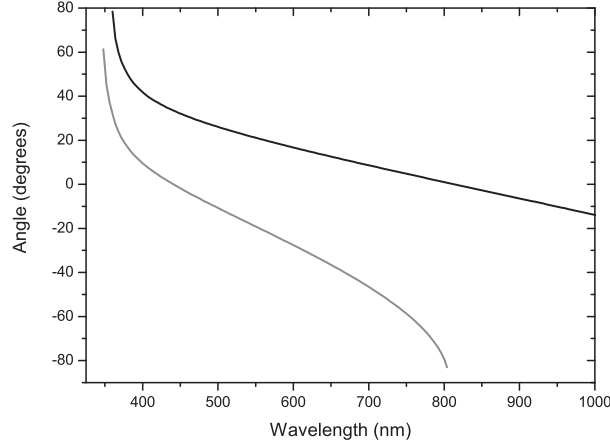


Figure 4.7: First order outcoupling angle vs. emission wavelength for 800 nm and 400 nm grating period (black and grey line respectively).

4.4 Measuring the propagation of surface plasmons

Investigation of the surface plasmon propagation length, has been done already, for large wavelengths and thus large propagation lengths [6]. To probe the propagation length at shorter wavelengths near the surface plasmon resonance frequency ω_{sp} is a real challenge, because one needs a high resolution excitation and detection technique due to the small propagation length of the surface plasmons in this regime. In this section Cathodoluminescence imaging spectroscopy is presented as a tool to study the propagation of surface plasmons near ω_{sp} . Figure 4.10 schematically shows the excitation of surface plasmons with an electron beam (diameter $< 10\text{nm}$), and the coupling to the far field via a grating in the metal.

The electron beam can excite the surface plasmon at a well defined distance from the the grating. By scanning away the electron beam from the grating, an intensity versus distance profile is obtained at a single wavelength. For each wavelength the intensity has a characteristic exponential decay, which increases for increasing wavelength. Figure 4.11 show the intensity profiles for both silver and gold and figure 4.12 shows the propagation distance of the surface plasmons as a function of the wavelength.

Figure 4.12 also shows a calculation for the propagation distance taking into account internal loss (black line), caused by the absorption in the film, which is given by [14]:

$$L_i = (2k_x'')^{-1} = \frac{c}{\omega} \left(\frac{\epsilon_m' + \epsilon_d}{\epsilon_m' \epsilon_d} \right)^{3/2} \frac{(\epsilon_m')^2}{\epsilon_m''}. \quad (4.7)$$

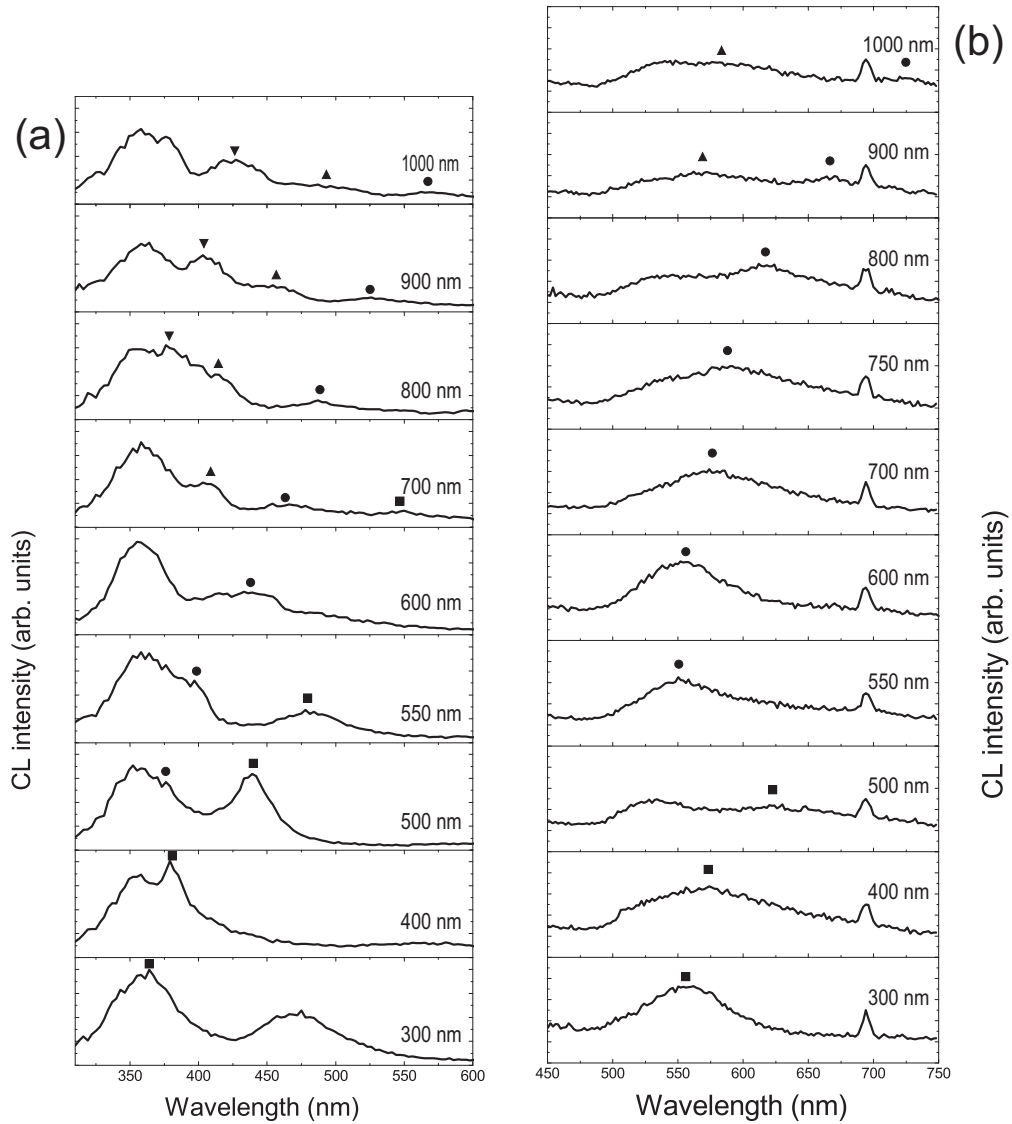


Figure 4.8: Measured CL spectra from gratings in silver (a) and gold (b), for different grating periods (indicated in figure). Apart from peaks near the plasmon resonance, which are present in each spectrum, several other maxima are detected, that are labelled with squares, circles and triangles. The maxima at 694 nm in (b) are due to Cr^{3+} pollution of the system.

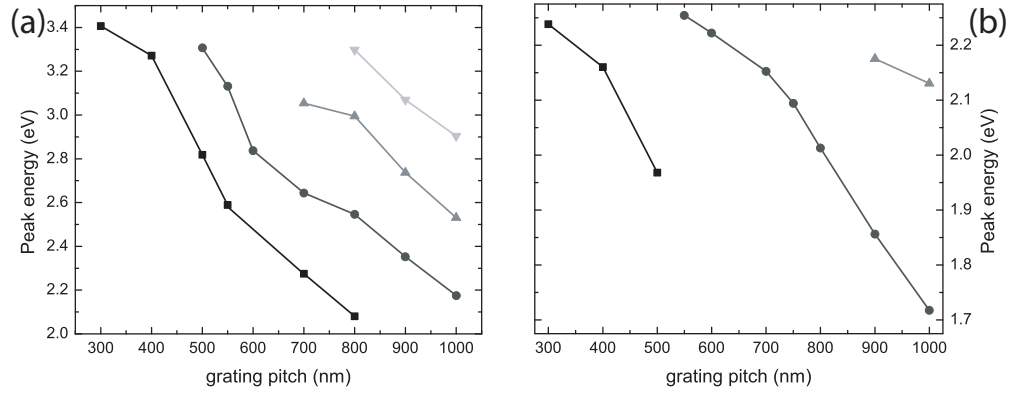


Figure 4.9: Peak energy versus the grating pitch silver (a) and gold(b). The used symbols correspond to the symbols used in fig. 4.8.

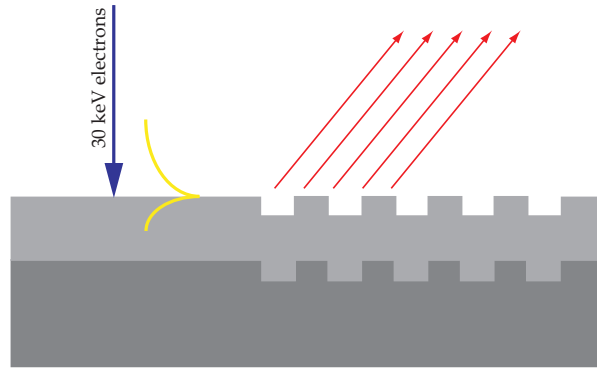


Figure 4.10: Excitation of surface plasmons near a grating, which couples the plasmon to the far field. By scanning away from the grating, an exponential decay in intensity is obtained, which $1/e$ decay length gives the characteristic propagation.

Measured data for ϵ_m are used. Clearly this calculation gives larger propagation lengths than the measured values. This implies that additional loss mechanisms play a role. The grey lines in figure 4.12 also takes scattering and radiation loss into account; due to roughness, the surface plasmon scatters to surface plasmons in a different direction, or couple to photons. These loss mechanisms are described by:

$$L_{sc} = \frac{2}{3} \frac{|\epsilon'_1|}{(\omega/c)^5} \frac{1}{\sigma^2 \delta^2}, \quad (4.8)$$

and

$$L_{rad} = \frac{3}{4} \frac{|\epsilon'_1|^{1/2}}{(\omega/c)^5} \frac{1}{\sigma^2 \delta^2}, \quad (4.9)$$

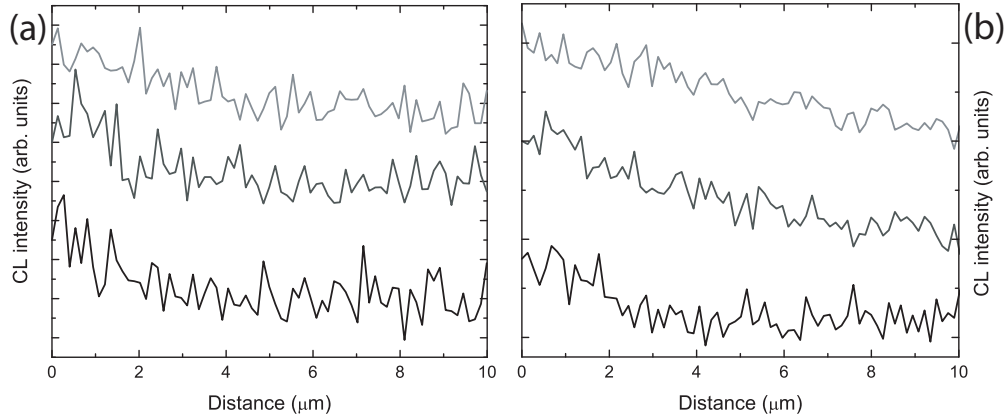


Figure 4.11: (a) CL line scans on silver, collected at 425 nm, 450 nm and 475 nm (black, dark grey and grey line respectively). (b) CL line-scans on gold, collected at 575 nm, 650 nm and 710 nm (black, dark grey and grey line respectively).

using measured values for σ and δ from AFM for the results from the silver film. The calculation reproduces the data for silver quite well for wavelengths between the plasmon resonance at 350 nm and 475 nm. For larger wavelengths an additional loss mechanism plays a role. Similarly for gold the measured data are all below the calculations taking internal loss into account, indicating that scattering and radiation due to surface roughness also are dominant loss processes. The calculation done is a best fit to the data points, with final values of $\sigma = 500$ nm and $\delta = 3.5$ nm.

One might wonder what the role of the backscattered electrons is in the measurements, since the typical propagation lengths of several μm is also the surface radius of backscattered electrons. These backscattered electrons can thus also reach the grating and excite the plasmons there. However there is no reason for this process to be wavelength dependent, while the data show an increase in propagation length of more than a factor of 20 between 550 and 710 nm for the gold film.

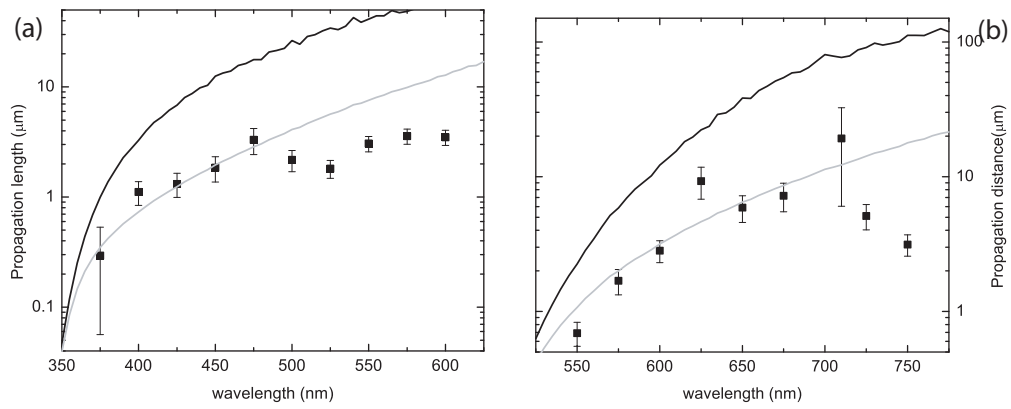


Figure 4.12: Propagation distance of surface plasmons on a metal film, measured (dots) and calculated (lines). The black line is the calculated propagation distance taking in to account the internal damping, the grey line also takes the roughness into account.

Chapter 5

Surface plasmons in metal nanoparticles

5.1 Introduction

Surface plasmons in metal nanoparticles are electron oscillations confined to the particles. For particles with diameter $d \ll \lambda$, the electrons start oscillating in phase with a plane excitation wave of wavelength λ . The electron oscillation, with the particle dipole plasmon frequency, produces a dipolar field outside the particle, which leads to an enhanced absorption and scattering cross section for electromagnetic waves, and also an strongly enhanced near field around the particle [19]. For larger particles also higher order modes will play a role, due to retardation effects. Although surface plasmons in particles are localized, there can be interaction between particles, which leads to a splitting of the plasmon peak, depending on the interparticle spacing. The spectral position of the peak for longitudinal modes will shift to the red, and for the transversal mode will slightly shift to blue. The interaction between particles can be used to make particle waveguides, in which the electromagnetic energy can be transported at subwavelength dimensions. At one end a plasmon is excited, which then couples to the other particles in the plasmon waveguide. [20] For such plasmonic nanostructures high resolution characterization is necessary, which can be achieved with CL imaging spectroscopy. In this chapter some preliminary results will be shown, from CL measurements on metal nanoparticles and metal shell particles. Also the excitation of surface plasmon resonances with electrons will be discussed.

5.2 Theory

The interaction between a fast moving electron and a metal nanoparticle leads to the emission of light, due to coupling of the electron and the plasmon modes in the particle. If an electron passes near a metal particle, the electric field generated by the electron can be decomposed in multipole components. Each component is scattered by the particle, giving rise to an induced or scattered electric field. This radiation is collected as the emission from the particle, and in case of energy loss measurements, this field is responsible for the loss, by acting back on the electron. An assumption of this model is that the electron does not pass through the particle, but passes near the particle. It will indeed be shown that the highest emission intensity will be obtained if an electron passes near the metal particle. Calculations are done for both relativistic electron velocities [21] and non-relativistic velocities, without considering size effects in the particle [22]. The energy loss in the non-relativistic case is given by:

$$\Gamma^{loss}(\omega) = \frac{4a}{\pi v^2} \sum_{l=1}^{\infty} \sum_{m=-l}^l \left(\frac{\omega a}{v} \right)^{2l} \frac{l}{(l+m)!(l-m)!} \times K_m^2 \left(\frac{\omega b}{v} \right) \text{Im} \left(\frac{\varepsilon - 1}{l\varepsilon + l + 1} \right), \quad ka \ll 1, \quad v/c \ll 1, \quad (5.1)$$

with a the diameter of the particle, b the impact parameter of the electron trajectory ($b > a$), v the electron speed and K_m the modified Bessel function. Figure 5.1 shows the loss probability for a 50 nm particle, with impact parameter of 52.5 nm and a 30 keV electron beam. At $\lambda = 500$ nm, $k/a \approx 0.6$ and for a 30 keV electron $v/c = 0.33$ which means that equation 5.1 is a reasonable approximation. The dielectric function ε is described by the Drude dielectric function

$$\varepsilon(\omega) = 1 - \frac{\omega_p^2}{\omega(\omega + i\eta)}, \quad (5.2)$$

with ω_p the plasma frequency and η the electron gas damping. The grey line in figure 5.1 is calculated with $\eta = 0.02 \omega_p$ and the black line with $\eta = 0.15 \omega_p$. The difference in damping factor has several consequences. For small damping, different multipole modes contribute to radiation, while for the large damping only the $l = 1$ or dipole mode contributes. The width of the peak increases drastically for large damping and the intensity decreases.

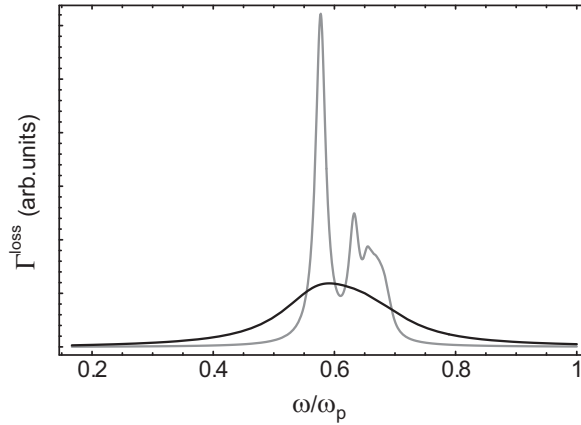


Figure 5.1: Loss probability for an electron passing near a 50 nm gold particle, calculated with a damping of $\eta = 0.02 \omega_p$ (grey line) and $\eta = 0.15 \omega_p$ (black line). The different peaks for the low damping calculation correspond to different multipole modes.

5.3 CL spectroscopy on single particles

Drops of nanoparticles in solution were deposited on a silicon substrate, where after drying, they lie isolated and in clusters. Particles were irradiated with an electron beam with a maximum energy of 30 keV, that was scanned over the region of interest. Figure 5.2 (a) shows a spectrum of a 110 nm gold particle, irradiated with a 30 keV electron beam. Several maxima are clearly visible, at 525 nm and 640 nm and a shoulder at 550 nm. The peak at 694 nm is attributed to emission from Cr^{3+} impurities (sapphire?) of the system. This result is in good agreement with the measurements done by Yamamoto *et al* on silver nanoparticles [18]. The different maxima are attributed to dipole and higher order multipole modes in the particle.

Figure 5.2 (b) shows a line scan, over the particle, collected at $\lambda = 525$ nm. The vertical dashed lines indicate the particle edges. This result clearly shows that the highest intensity is obtained when an electron passes near a particle. Again this is in good agreement with earlier measurements on silver particles [18].

Measurements performed on smaller gold particles show different behavior. Figure 5.3 shows the spectrum and a line scan ($\lambda = 540$ nm) from a 45 nm gold particle. The spectrum only shows a single peak at 550 nm and the linescan does not show the same characteristic shape as in figure 5.2 (b), but again excitation occurs when the electron beam passes near the particle.

Figure 5.4 shows the spectra of silica/gold/silica core/shell/shell parti-

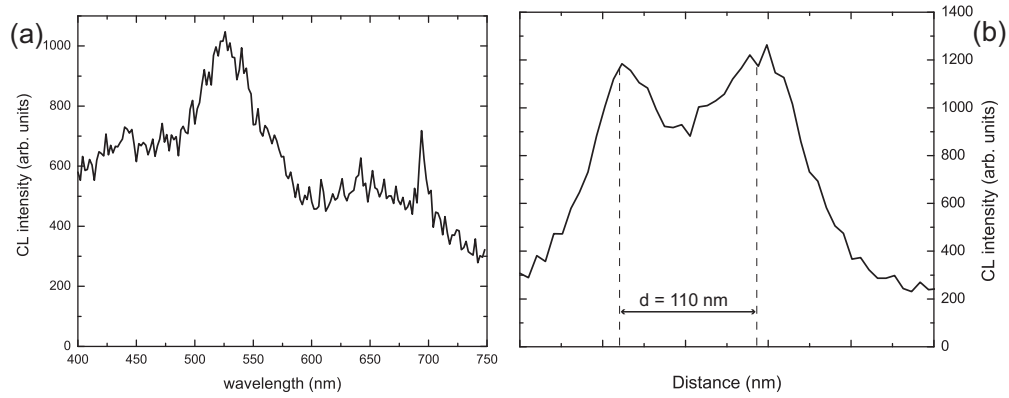


Figure 5.2: (a) CL spectrum from gold nanoparticle ($d = 100$ nm), with maxima at 525 and 640 nm. (The peak at 694 nm is attributed to emission of Cr^{3+} impurities.) (b) CL line scan over the particle, collected at $\lambda = 525$ nm, showing excitation of modes when the beam passes near the particle.

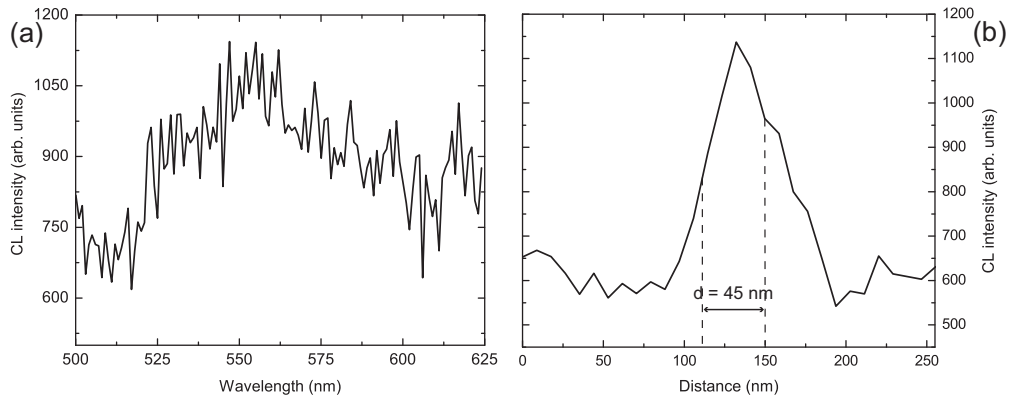


Figure 5.3: (a) CL spectrum of small (50 nm) gold particle. (b) CL linescan over the particle, collected at $\lambda = 540$ nm.

cles, both spherical shaped (black line) and deformed by ion beam irradiation (grey line) (fabrication: see ref [23] and cited references therein). The undeformed particle has a maximum at $\lambda = 625$ nm, which is in agreement with optical extinction measurements [23]. The maximum for the deformed particle is clearly blueshifted with respect to the undeformed particle.

5.4 Coupling between metal nanoparticles

As mentioned in section 5.1 surface plasmons in metal nanoparticles can interact with neighboring particles, leading to a splitting of the surface plasmon peak [24]. CL is used to measure the shift of the plasmon peak due to cou-

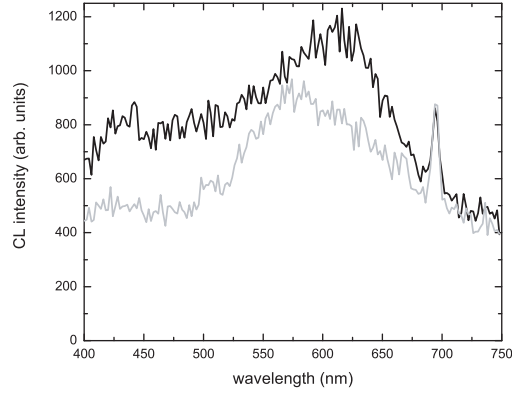


Figure 5.4: CL spectra from undeformed (black line) and deformed (grey line) silica/gold/silica core/shell/shell particles. The spectrum from the deformed particle is clearly blueshifted with respect to the undeformed particle.

pling between particles. A tilted sample was used, to excite both longitudinal and transversal modes in the particles. Figure 5.5 show spectra from a single particle (grey line, same spectrum as shown in figure 5.3) and a cluster of many particles (black line). A small red shift in the spectrum from the cluster is observed, which is attributed to longitudinal coupling of surface plasmons between the particles. A splitting of the peak is not observed, which may be attributed to the fact that the blue shift of the plasmon peak, due to transversal coupling is much weaker than the redshift due to longitudinal coupling.

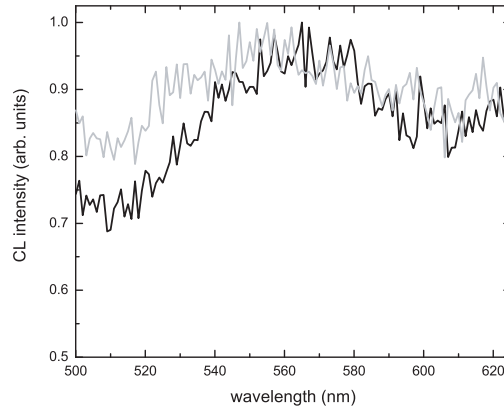


Figure 5.5: CL spectra from single gold particle (black line) and a cluster of many particles (grey line), with diameter $d = 50$ nm. The spectrum from the cluster of particles is slightly redshifted, which is attributed to longitudinal plasmon coupling between the particles.

Bibliography

- [1] Yacobi B.G. and Holt D.B. *Cathodoluminescence scanning electron microscopy of semiconductors*. J. Appl. Phys., **59**(4), R1 (1986)
- [2] Ponce F.A., Bour D.P., Götz W. and Wright P.J. *Spatial distribution of the luminescence in GaN thin films*. Appl. Phys. Lett, **68**(1), 57 (1996)
- [3] Fan H.J., Bertram F., Dadgar A., Christen J., Krost A. and Zacharias M. *Self-assembly of ZnO nanowires and the spatial resolved characterization of their luminescence*. Nanotech., **15**, 1401–1404 (2004)
- [4] Ritchie R.H. *Plasma losses by fast electrons in thin films*. Phys. Rev., **106**(5), 874 (1957)
- [5] Powell C.J. and Swan J.B. *Origin of the characteristic electron energy loss in aluminium*. Phys. Rev., **115**(4), 870 (1959)
- [6] Weeber J.C., Krenn J.R., Dereux A., Lamprecht B., Lacroute Y. and Goudonnet J. *Near-field observation of surface plasmon polariton propagation on thin metal stripes*. Phys. Rev. B., **64**, 45411 (2001)
- [7] de Dood M.J.A., Berkhout B., Kats C.M., Polman A. and van Blaaderen A. *Acid-based synthesis of monodisperse rare-earth-doped colloidal SiO₂ spheres*. Chem. Mater., **14**, 2849–2853 (2002)
- [8] Ishikki H., de Dood M.J.A., Polman A. and Kimura T. *Self-assembled infrared luminescent Er-Si-O crystallites on silicon*. Appl. Phys. Lett, **85**, 4343 (2004)
- [9] Polman A. *Erbium implanted thin film photonic materials*. J. Appl. Phys., **82**(1), 1–39 (1997)
- [10] Kanaya K. and Okayama S. *Penetration and energy-loss theory of electrons in solid targets*. J. Phys. D., **5**, 43 (1972)

- [11] Everhart T.E. and Hoff P.H. *Determination of kilovolt electron energy dissipation vs penetration distance in solid materials.* J. Appl. Phys., **42**(13), 5837 (1971)
- [12] Klein C.A. *Bandgap dependence and related features of radiation ionization energies in semiconductors.* J. Appl. Phys., **39**(4), 2029 (1968)
- [13] Davidson S.M. and Dimitriadis C.A. *Advances in the electrical assessment of semiconductors using the scanning electron microscope.* J. Microsc., **118**, 275 (1980)
- [14] Raether H. *Surface plasmons on smooth and rough surfaces and on gratings* (Springer-Verlag, 1986)
- [15] Ferrell R.A. *Predicted radiation of plasma oscillations in metal films.* Phys. Rev., **111**(5), 1214 (1958)
- [16] Palik E.D. *Handbook of optical constants of solids* (Academic press, New York, 1985)
- [17] Johnson P.B. and Christy R.W. *Optical constants of the noble metals.* Phys. Rev. B, **6**(12), 4370 (1972)
- [18] Yamamoto N., Araya K. and García de Abajo F.J. *Photon emission from silver particles induced by a high-energy electron beam.* Phys. Rev. B., **64**, 205419 (2001)
- [19] Maier S.A. and Atwater H.A. *Plasmonics: Localization and guiding of electromagnetic energy in metal/dielectric structures.* J. Appl. Phys, **98**, 011101 (2005)
- [20] Maier S.A., Kik P.G., Atwater H.A., Meltzer S., Harel E., Koel B.E. and Requicha A.A.G. *Local detection of electromagnetic energy transport below the diffraction limit in metal nanoparticle plasmon waveguides.* Nat. Mater, **2**, 229 (2003)
- [21] García de Abajo F.J. *Relativistic energy loss and induced photon emission in the interaction of a dielectric sphere with an external electron beam.* Phys. Rev. B., **59**(4), 3095 (1999)
- [22] Ferrell T.L. and Echenique P.M. *Generation of surface excitations on dielectric spheres by an external electron beam.* Phys. Rev. Lett, **55**(14), 1526 (1985)

-
- [23] Penninkhof J.J., Graf C., van Dillen T., Vredenberg A.M., van Blaaderen A. and Polman A. *Angle-dependent excitation of anisotropic silica/au core/shell colloids made via ion irradiation*. Adv. Mater., **17**, 1484–1488 (2005)
- [24] Maier S.A., Kik P.G. and Atwater H.A. *Optical pulse propagation in metal nanoparticle chain waveguides*. Phys. Rev. B., **67**, 205402 (2003)

Acknowledgements

At the end of my masters project at AMOLF, I would like to thank many people, who helped me to successfully end my research project and made this year at AMOLF a very pleasant time. First of all, I would like to thank Albert Polman, for his ideas and inspiration, and of course for giving me the opportunity to buy a very expensive new instrument, the cathodoluminescence spectrometer. I also would like to thank all the members of the photonic materials group: Hans Mertens, Joan Penninkhof, Martin Kuttge, Ewold Verhagen, Sébastien Bidault (for the nice coffee breaks in the sun), Femius Koenderink, Jeroen Kalkman, Anna Tchebotareva, Martien den Hertog, Teun van Dillen and my room mates Rob van Loon and René de Waele (especially for being such an enthusiastic partner during our experiments on the metal nanoparticles). I would like to thank Harry Atwater and Carrie Ross for the useful discussions during your stay at AMOLF. Your results helped me understand my own results much better. I really want to thank the technicians Johan Derks and even more Hans Zeijlemaker, you were a great support during the installation and start up period of the system and therefore attributed a lot to the success of this project. Also thanks to Chris Retif for suggestions during the fabrication of my samples.

Ik wil natuurlijk ook mijn familie en vrienden thuis bedanken die mij bewust of onbewust gesteund hebben. En daarbij gaat de meeste dank naar mijn ouders, die mijn studie mogelijk gemaakt hebben. Voor jullie belangstelling en ondersteuning ook als ik het eens wat minder zag zitten ben ik jullie voor altijd dankbaar.